

Full length article

Design of independent and radiation modulation enhanced electrochromic windows in visible and infrared ranges

Xueyu Wang^a, Shuo Chen^a, Yumin Liu^a, Tiesheng Wu^{b,*}, Jing Li^a, Danfeng Zhu^c, Yuhang Sun^a, Hongjie Fan^a^a Beijing University of Posts and Telecommunications, State Key Laboratory of Information Photonics and Optical Communications, No.10, Xitucheng Road, Beijing, 100876, China^b Guilin University of Electronic Technology, College of Information and Communication Engineering, 1 Jinji Road, Guilin, 541004, China^c School of Physics and Electrical Engineering, Jiaying University, Meizhou 514015, China

ARTICLE INFO

Keywords:

Electrochromic

Electro-optical

Visible

Infrared

Multilayer

ABSTRACT

Electrochromic windows regulate the transmission and absorption of sunlight according to environmental conditions and personal preferences, resulting in energy conservation. However, developing smart windows that can independently modulate visible and infrared (IR) radiation remains a significant challenge. This paper presents a multilayer film structure for electrochromic windows based on the electro-optic dielectric material of 4-dimethyl-amino-N-methyl-4-stilbazoliumtosylate (DAST), and the film modulates visible and IR light individually. The refractive indices of multilayer DAST films change when different bias voltages are applied, which alters the structure's impedance and selectively modulates electromagnetic wave transmission. Simulation results indicate that the smart window can independently modulate the integrated visible transmittance (T_{vis}) and integrated infrared transmittance (T_{IR}) at four different bias voltages (-20 V to +20 V). The modulation ranges for T_{vis} and T_{IR} are 72.5% to 92.3% and 46.1% to 95.2%, respectively, and the theoretical results surpass those of recent works. A fully-connected network with position coding is employed here, and simulation time is reduced based on truth prediction data. The multilayer structure proposed enables independent modulation of visible and IR light, making it a promising candidate for smart windows since it is lithography-free, large-area compatible, and polarization-independent.

1. Introduction

In recent decades, the issue of global warming and the energy crisis has garnered significant attention due to the massive combustion of fossil fuels. Saving energy has become a hot research topic. Between 40% and 50% of the world's total energy consumption is currently attributed to building energy consumption, with lighting, ventilation, heating, and air conditioning being the primary sources [1,2]. Traditional windows are passive as they allow heat and light to enter and leave the building without control, resulting in considerable energy consumption [3]. Smart windows are gaining attention for their ability to artificially alter the direction and intensity of electromagnetic radiation based on seasonal changes and individual preferences, saving energy. The rapid development of smart windows technology has resulted in various modulation mechanisms, such as thermochromic

[4,5], photochromic [6,7], electrochromic [8,9], and mechanochromic [10,11] windows. Electrochromic and mechanochromic windows that can dynamically adjust their transmittance in response to human demand have garnered attention. Mechanochromic windows have limited applications due to their short working life and low mechanical strength [2]. Electrochromic windows are employed in buildings [12,13], cars [14], and airplanes [15] owing to their exceptional long-term cycle stability, extended working life, and ability to offer occupants privacy and comfort. Aalizadeh et al. introduced an ultra-thin Ag-DAST-Ag structure that controls visible light intensity by changing bias voltages [16]. Chowdhary et al. developed electrochromic smart windows that use an electro-optic effect to dynamically regulate the intensity of transmitted solar radiation [17–19]. Forouzmand et al. designed an electro-optical amplitude modulator capable of modifying two bias voltages and exciting a strongly coupled guided-mode resonance,

* Corresponding author at: Guilin University of Electronic Technology, College of Information and Communication Engineering, 1 Jinji Road, Guilin, 541004, China.

E-mail addresses: microliuyumin@hotmail.com (Y. Liu), tieshengw@guet.edu.cn (T. Wu).

<https://doi.org/10.1016/j.optlastec.2023.109774>

Received 5 March 2023; Received in revised form 19 June 2023; Accepted 24 June 2023

Available online 10 July 2023

0030-3992/© 2023 Elsevier Ltd. All rights reserved.

achieving a relatively high reflection amplitude within the 0.45–0.6 μm range [20]. The design of the electrochromic window using two bias voltages [20] offers a new approach. Additionally, experiments have demonstrated that electrochromic smart windows can effectively regulate solar radiation [8,21,22]. However, the previously reported electrochromic windows cannot independently modulate visible and IR light, limiting their practical application.

To address the gap in the literature, we introduce multilayer film smart windows based on DAST, which can independently modulate visible and IR light. Applying differing bias voltages to multilayer DAST films results in changes to refractive indices and structural impedance, enabling selectively visible and IR light transmission. Employing a fully-connected network with position encoding considerably decreases simulation duration. The results demonstrate that applying four different bias voltages to the electrochromic windows can individually control the T_{vis} and T_{IR} within 72.5% – 92.3% and 46.1% – 95.2%, respectively. The multilayer structure can independently modulate visible and IR light and provides a promising approach for smart windows due to its lithography-free, large-area compatibility, and polarization independence.

2. Physical principles of controlling solar radiation

Solar radiation at the Earth's surface consists of 53% infrared (λ greater than 700 nm), 43% visible ($400 \text{ nm} < \lambda$ less than 700 nm), and 4% ultraviolet (λ less than 400 nm) [23]. Smart windows are mainly regulated for T_{vis} and T_{IR} , and their four main operational modes, namely mode - I, II, III, and IV, which are described below:

Mode - I: visible blocked and IR allowed, as shown in Fig. 1(a). This setting provides a warm and dark environment and is suitable for winter sleepers.

Mode - II: visible and IR allowed, as displayed in Fig. 1(b). This setting is suitable for application during cold winter days as it allows solar energy entry into the building, providing warmth.

Mode - III: visible and IR blocked, as illustrated in Fig. 1(c). This configuration can keep the building dark and cool while preventing sunlight transmission.

Mode - IV: visible allowed and IR blocked as in Fig. 1(d). This condition can maintain room brightness while reducing temperature increases during hot summer days.

Mode - I and II are more suited to hot summer days, while mode - III and IV are exceptionally equipped for chilly winter days. In addition to these four modes, smart windows should be able to adjust visible

and IR light separately to accommodate individual preferences and seasonal conditions. As shown in Fig. 1(e), the ideal regulation range for smart windows is 0—100% for both T_{vis} and T_{IR} (represented by the light blue section in the figure).

3. Materials and methods

The transfer matrix method (TMM) [17,24] calculates the reflection and transmission of multilayer film electrochromic windows. Its characteristic matrix identifies the interaction between each film layer and electromagnetic wave. The characteristic matrix of the j -layer film layer can be expressed as follows [19,25,26]:

$$M_j = \begin{bmatrix} \cos\delta_j & \frac{is\sin\delta_j}{\eta_j} \\ i\eta_j\sin\delta_j & \cos\delta_j \end{bmatrix} \quad (1)$$

where $\delta_j = 2\pi n_j d_j \cos\theta_j / \lambda$, $\eta_j = n_j \varepsilon_0 / \mu_0 \cos\theta_j$ (for TE (Transverse Electric)-polarization) or $\eta_j = n_j \varepsilon_0 / \mu_0 / \cos\theta_j$ (for TM (Transverse Magnetic)-polarization). λ is the wavelength, d_j , n_j , and θ_j are the thickness, refractive index, and propagation angle of the j layer medium, respectively. ε_0 is the vacuum permittivity, μ_0 is the vacuum magnetism. The N -layer structure characteristic matrix is:

$$M = \prod_{j=1}^N M_j = \begin{bmatrix} m_{11} & m_{12} \\ m_{21} & m_{22} \end{bmatrix} \quad (2)$$

According to Eq. (2), the reflection (r) and transmission (t) coefficients of the structure are:

$$r = \frac{\eta_0 m_{11} + \eta_0 \eta_t m_{12} - m_{21} - \eta_t m_{22}}{\eta_0 m_{11} + \eta_0 \eta_t m_{12} + m_{21} + \eta_t m_{22}} \quad (3)$$

$$t = \frac{2\eta_0}{\eta_0 m_{11} + \eta_0 \eta_t m_{12} + m_{21} + \eta_t m_{22}} \quad (4)$$

where η_0 and η_t are the modified admittance of electromagnetic wave input and outgoing port, respectively. The reflection (R) and transmittance (T) can be represented as $R = |r|^2$ and $T = n_t \cos\theta_t |t|^2 / (n_i \cos\theta_i)$ (for TE-polarization) or $T = n_t \cos\theta_t |t|^2 / (n_i \cos\theta_i)$ (for TM-polarization), respectively [27]. The n_i and n_t are the refractive indexes of the incident medium and the outgoing medium, and the θ_i and θ_t are the incident and refraction angles. The absorption can be calculated as $A = 1 - R - T$.

The DAST material exhibits a high electro-optical factor (3.41 nm/V), providing exceptional tunability with bias voltage. As shown by

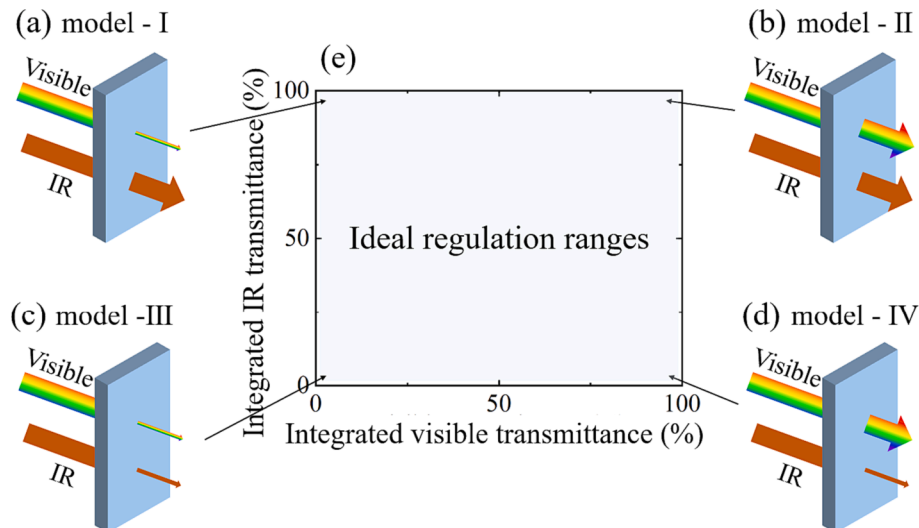


Fig. 1. Four common operation modes for smart windows (a - d), and the T_{vis} and T_{IR} regulation range for smart windows (e).

previous research [16,28], its refractive index (n_{DAST}) can be modeled as a function of the applied voltage:

$$n_{\text{DAST}} = n_0 + \frac{dn}{du} \frac{V}{t_{\text{DAST}}} \quad (5)$$

where $n_0 = 2.2$ is the refractive index at zero bias voltage, V is the applied bias voltage, and t_{DAST} represents the DAST thickness. The electro-optical coefficient of DAST is $\frac{dn}{du} = 3.41 \text{ nm/V}$. Among the three most common transparent conductive oxides (indium tin oxide (ITO), aluminum-doped zinc oxide (AZO), and aluminum oxynitride (ALON)), ALON is selected to be employed in the proposed structure due to its durability, lightweight, and low cost [29]. The refractive index of ALON is taken from data [30], and the refractive index of PMMA (polymethyl methacrylate) is obtained from experimental data [31]. The integrated visible transmittance (T_{vis}) and integrated infrared transmittance (T_{IR}) are defined as follows:

$$T_{\text{vis}} = \frac{\int_{400}^{700} \Phi_{\text{sol}}(\lambda) T(\lambda) d\lambda}{\int_{400}^{700} \Phi_{\text{sol}}(\lambda) d\lambda} \quad (6)$$

$$T_{\text{IR}} = \frac{\int_{700}^{2500} \Phi_{\text{sol}}(\lambda) T(\lambda) d\lambda}{\int_{700}^{2500} \Phi_{\text{sol}}(\lambda) d\lambda} \quad (7)$$

where Φ_{solar} refers the solar irradiance spectrum for an air mass of 1.5 [23].

4. Results

4.1. Electrochromic window with one bias voltage

Fig. 2(a) depicts the three-dimensional schematic diagram of the three-layer electrochromic device. The device comprises three layers, with ALON as the top and bottom layers and a middle layer made of DAST, which exhibits a high electro-optical coefficient. The structure's thickness is d_1 , d_2 , and d_3 from top to bottom. Electromagnetic wave reflect back and forth at the DAST-ALON interface due to the difference in refractive index between the two materials. Therefore, the three-layer

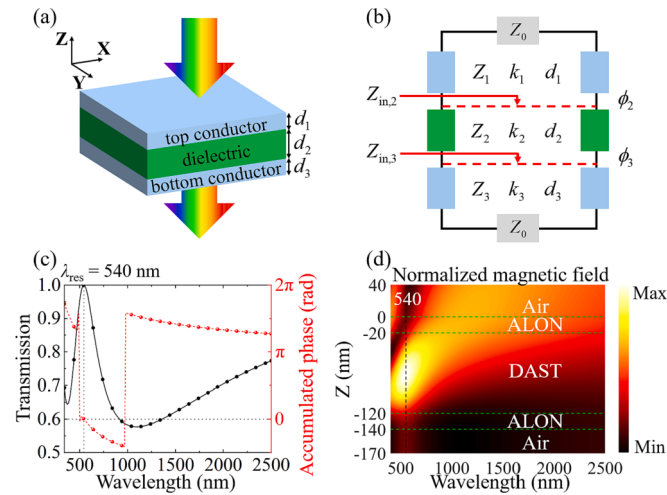


Fig. 2. (a) The schematic of the electrochromic glass with one bias voltage. (b) The circuit model employs transmission line theory (TLM) with electromagnetic wave incidents from above. (c) Black solid lines represent the transmission spectrum, and the phase is shown with red dashed lines. The resonant wavelength (λ_{res}) of 540 nm is correctly predicted by TLM (shown with a red dotted line) when the accumulated round trip phase equals zero (indicated by black dotted cross lines). (d) The normalized magnetic field is a function of wavelength. A vertical dashed line indicates the Fabry-Perot cavity's resonant wavelength ($\lambda_{\text{res}} = 540 \text{ nm}$). (For interpretation of the references to color in this figure legend, the reader is referred to the web version of this article.)

configuration can be considered a Fabry-Perot cavity. When the wavelength of incident light coincides with the resonant wavelength of the cavity, electromagnetic wave are allowed to enter the structure, and transmission reaches a peak. The Fabry-Perot cavity is described by [32]:

$$2 \left(\frac{2\pi}{\lambda_{\text{res}}} \right) n_2 d_2 + 2\Phi = 2\pi m \quad (8)$$

where λ_{res} is the resonance wavelength, and m is an integer number that determines the order of the cavity mode. The Φ represents the phase shift after reflection from both sides of the dielectric layer. For the ALON-DAST-ALON structure, $d_1 = 20 \text{ nm}$, $d_2 = 100 \text{ nm}$, and $d_3 = 20 \text{ nm}$. The circuit model is shown in Fig. 2(b) is based on transmission line theory and provides a more comprehensive investigation of the resonant wavelength of the transmission spectrum. Z_1 , Z_2 , and Z_3 are the normalized characteristic impedance of the top conductor, dielectric, and bottom conductor. k_1 , k_2 and k_3 are the propagation constant of the top conductor, dielectric, and bottom conductor, respectively. Z_0 is the free-space normalized impedance, and its value is 1. The input impedance seen at the interface between the top conductor and the dielectric, as seen from above, is denoted by $Z_{\text{in},2}$ and $Z_{\text{in},3}$, respectively, and can be calculated using the formula below [33]:

$$Z_{\text{in},3} = Z_3 \frac{Z_0 - jZ_3 \tan(k_3 t_3)}{Z_3 - jZ_0 \tan(k_3 t_3)} \quad (9)$$

$$Z_{\text{in},2} = Z_2 \frac{Z_{\text{in},3} - jZ_2 \tan(k_2 t_2)}{Z_2 - jZ_{\text{in},3} \tan(k_2 t_2)} \quad (10)$$

The reflection coefficients (r_3 and r_2) corresponding to both sides of the intermediate dielectric layer can be expressed as follows:

$$r_3 = Z_3 \frac{Z_{\text{in},3} - Z_2}{Z_{\text{in},3} + Z_2} = |r_3| \angle \phi_3 \quad (11)$$

$$r_2 = Z_2 \frac{Z_{\text{in},2} - Z_2}{Z_{\text{in},2} + Z_2} = |r_2| \angle \phi_2 \quad (12)$$

where ϕ_3 and ϕ_2 indicate the phase shift at the ALON-DAST interface reflections, respectively, in Eq. (8), the Φ is equal to $\phi_3 + \phi_2$. In Fig. 2(c), solid black lines represent the transmission spectra, and red dashed lines indicate the phase. When the accumulated round trip phase is 0, the maximum transmission equals 99.9%, which matches the transmission peak obtained through TMM. Fig. 2(d) illustrates the ALON-DAST-ALON structure's normalized magnetic field distribution over 400—2500 nm. The magnetic field is enhanced and restricted inside the structure, and the device supports a cavity resonance mode at $\lambda = 540 \text{ nm}$, corresponding to the vertical curve.

Fig. 3(a) demonstrates the electrochromic window diagram with one bias voltage. Fig. 3(b) and (c) illustrate the effects of thickness (d_2) and bias voltage variations on visible and IR ranges. The light cyan and light purple areas indicate the solar radiation spectrum and the visibility function of human eyes, respectively. Thin-film interference significantly impacts transmission and reflection in the multilayer system. According to Eq. (8), when the accumulated round trip phase in the DAST equals zero, the interference between the top and bottom surfaces can lead to anti-reflectance, reducing the reflected light [34]. According to Eq. (8), Fig. 3(b) and (c) display that the resonance peak (λ_{res}) is red-shifted as the applied bias voltage and d_2 increase. Fig. 3(d) plots the T_{vis} and T_{IR} of the ALON-DAST-ALON structure at different bias voltages. The construction exhibits $T_{\text{vis}} = 93.0\%$ and $T_{\text{IR}} = 85.3\%$ with a bias voltage of -20 V , which is mode - II. As the bias voltage increases, both T_{vis} and T_{IR} decrease substantially. When the applied bias voltage equals $+20 \text{ V}$, T_{vis} reaches 75.0% while T_{IR} becomes 47.6% . The summer months with high sunlight intensity are suitable for using this mode. During the production of multilayer films, the thickness can vary for various reasons, resulting in changes in the structure's properties. Here it is assumed that d_1 , d_2 and d_3 each produce a thickness error of 10%

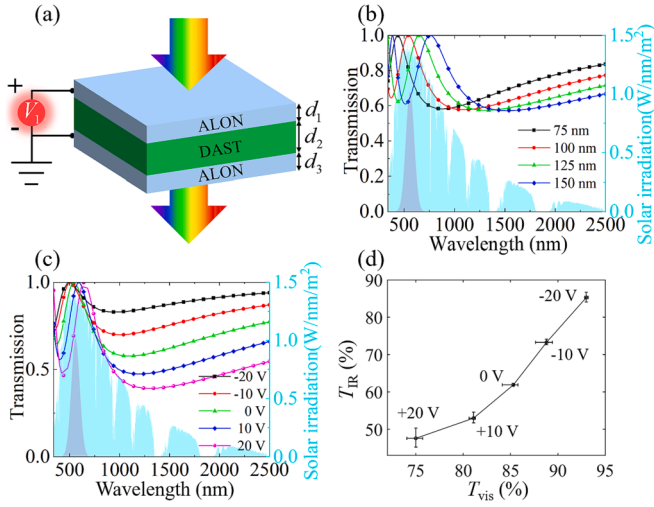


Fig. 3. (a) The schematic of the electrical glass with bias voltage. The transmission spectrum of smart glass versus d_2 (b) and bias voltage (c). (d) The T_{vis} and T_{IR} as a function of bias voltage. The error bars represent the effect on T_{vis} and T_{IR} of a 10% thickness error generated by d_1 , d_2 and d_3 .

during the production process, and the error bars in Fig. 3(d) illustrate the impact of thickness error on T_{vis} and T_{IR} . The limited modulation range of the electrochromic window of the ALON-DAST-ALON structure makes it challenging to implement in practice.

4.2. Electrochromic window with two bias voltages

Fig. 4(a) illustrates a configuration with two bias voltages, which provides an electrochromic window with a wide range of adjustment. DAST and ALON films are alternated in this structure, with $d_{DAST} = 100$ nm and $d_{ALON} = 20$ nm thicknesses, respectively. The electrochromic window can modify the structure's impedance in the visible and infrared ranges by modulating the refractive index of DAST in the top and bottom layers with two different bias voltages, regulating T_{vis} and T_{IR} .

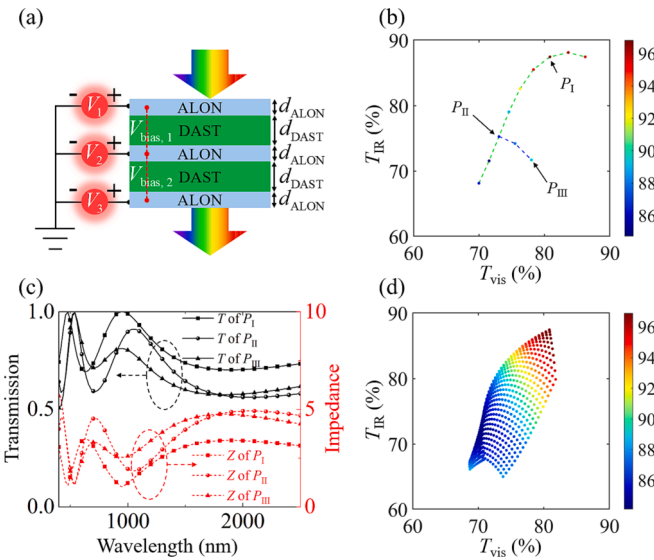


Fig. 4. (a) Diagram of an electrochromic window with two bias voltages. (b) Relationship between the electrochromic window's T_{vis} , T_{IR} , and CRI and two bias voltages. The $V_{bias,1}$ and $V_{bias,2}$ of P_I are +10 V and -10 V, respectively. The $V_{bias,1}$ and $V_{bias,2}$ of P_{II} are -10 V and +10 V, respectively. The $V_{bias,1}$ and $V_{bias,2}$ of P_{III} are -20 V and +10 V, respectively. (c) The transmission and impedance of P_I , P_{II} , and P_{III} . (d) The T_{vis} , T_{IR} , and CRI function as the two bias voltages ($V_{bias,1}$ and $V_{bias,2}$).

independently and effectively. Fig. 4(b) displays the smart window at different bias voltages for T_{vis} , T_{IR} , and color rendering index (CRI), and the color-coded scale shows CRI variations. The $V_{bias,i} = V_i - V_{i+1}$. The green and blue dashed lines represent $V_{bias,1} = -10$ V, and $V_{bias,2} = +10$ V, respectively. The refractive index of the top layer of DAST is 1.859 when $V_{bias,1}$ is set to -10 V. The variation in $V_{bias,2}$ leads to a change in the impedance of the structure, altering the transmission spectrum, as shown in Fig. 4(c). This effect is illustrated in the $T_{vis} - T_{IR}$ diagram, including points P_I and P_{II} , with a green dashed line. The difference in T_{vis} and T_{IR} between P_{II} and P_{III} is caused by the varying refractive indices and impedance of their top DAST layers, resulting from their differing $V_{bias,1}$ despite having the same $V_{bias,2}$. P_I , P_{II} , and P_{III} configurations have different bias voltages, eventually leading to T_{vis} , T_{IR} , and CRI differences. Thus, increasing the range of variation for $V_{bias,1}$ and $V_{bias,2}$ will further expand the control range of the smart window's T_{vis} and T_{IR} . Fig. 4(d) illustrates the impact of varying $V_{bias,1}$ and $V_{bias,2}$ from -10 V to +10 V (step = 1 V) on T_{vis} , T_{IR} , and CRI. The region covered by the colored plot in the diagram represents the control range of T_{vis} and T_{IR} for the smart window. The T_{vis} and T_{IR} regulation range of the electrochromic window can be significantly increased by increasing the number of bias voltages and the range of bias voltage regulation.

4.3. Electrochromic window with multiple bias voltages

Fig. 5(a), (c), and (e) display schematic diagrams of structures with 3, 4, and 5 bias voltages for electrochromic windows. The voltage range applied to the transparent conductive ALON is -10 V to +10 V in

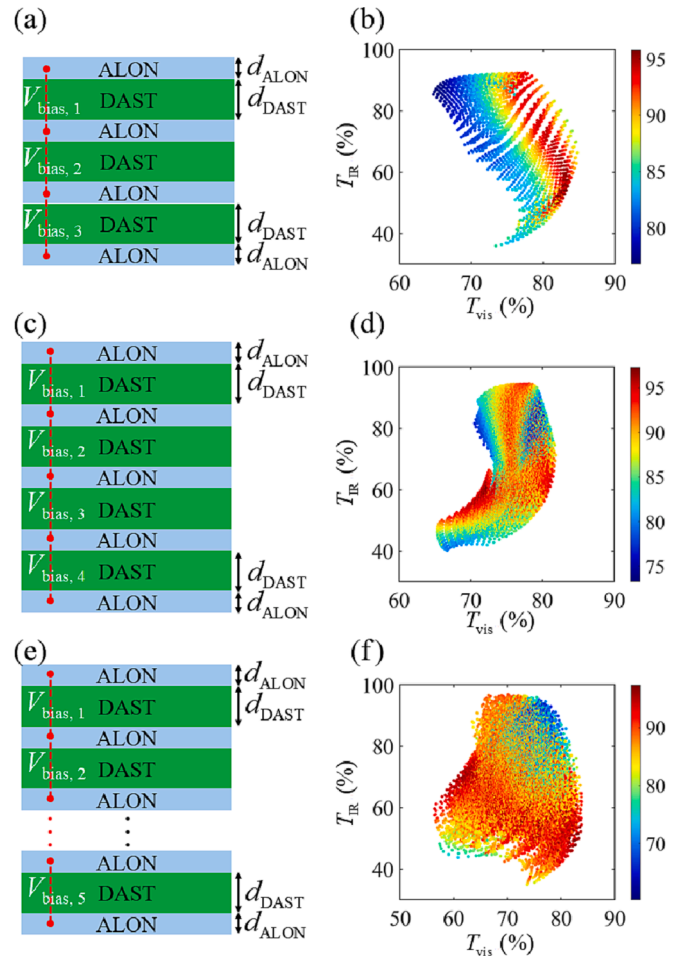


Fig. 5. (a) Diagram of the structure of an electrochromic window with three (a), four (c), and five (e) bias voltages. The T_{vis} , T_{IR} , and CRI as a function of three (b), four (d), and five (f) bias voltages.

increments of 2 V. The d_{ALON} and d_{DAST} were set to 20 and 100 nm, respectively. Fig. 5(b), (d) and (f) demonstrate that the adjustable range of the smart window increases gradually with an increase in the number of bias voltages. It is critical to recall that Fig. 5(f) is derived from the fully-connected network prediction, and the prediction details are provided below. Besides, Figure S1 (Supporting Information) displays T_{vis} , T_{IR} , CRI, transmission, and impedance for electronic windows under five bias voltages.

4.4. Fully-connected network acceleration simulation

Expanding the number of bias voltages applied to the structure will increase the electrochromic window's adjustable range. However, the simulation time will increase due to extensive calculations. This work presents a fully-connected network that uses position coding to anticipate data based on truth values, reducing simulation time and achieving the maximum modulation range of T_{vis} and T_{IR} . The general data input approach has recently converted binary values into networks [35]. However, an alternative method, positional encoding, can enhance the dimensionality of input coordinates and enable accelerated learning for fully-connected deep networks [36]. The positional encoding equation is defined as follows:

$$\text{Input}(p) = (\sin(2^0 p), \cos(2^0 p), \dots, \sin(2^{L-1} p), \cos(2^{L-1} p)) \quad (13)$$

where the $\text{Input}(\cdot)$ represents the input parameter normalized to the range [0, 1], the transformed high-frequency function is located on the right-hand side of the equation, and L equals 12. The process of converting $V_{\text{bias},i}$ to $\widetilde{V}_{\text{bias},i}$ is shown in Fig. 6.

As shown in Fig. 6, the network inputs are $V_{\text{bias},1}$, $V_{\text{bias},2}$, $V_{\text{bias},3}$, and $V_{\text{bias},4}$ and the network outputs are T_{vis} , T_{IR} , and CRI. An electrochromic window with four bias voltages is an example of this network prediction process. The V_1 , V_2 , V_3 , V_4 , and V_5 of the structure range from -10 V to $+10$ V with a step of 4 V. Excluding the repeated bias voltage combinations, there are 4651 states, and TMM obtains these states' T_{vis} , T_{IR} , and CRI. The 4651 data was partitioned into three groups, namely training (80%), validation (10%), and testing (10%) datasets. The network prediction method was trained using an Nvidia GTX 1650 graphics card with 4 GB of memory. The 4651 states with different T_{vis} , T_{IR} , and CRI are shown in Fig. 7(a). By changing the step size to 2 V and removing repeated bias voltage combinations, the total number of states is 61051. Fig. 7(b) depicts the 61,051 states obtained via the TMM. The T_{vis} , T_{IR} , and CRI of 61,051 states predicted by the fully-connected network are shown in Fig. 7(c). The mean square error (MSE) calculates the average loss over the output by summing the squared differences between the true and predicted values. The MSE values for T_{vis} , T_{IR} , and CRI are 0.000142, 0.000622, and 7.21, respectively, indicating the model's accuracy. The TMM calculates 61,051 states in approximately 4 h. In contrast, the fully-connected network takes only about 16

min (5 min for computing 4651 states using TMM, 11 min for network training, and 3 s for network prediction). The results demonstrate that network prediction effectively reduces simulation time while maintaining accurate computation.

5. Discussion

5.1. Methods to improve CRI

Covering the design with PMMA reduces electromagnetic wave reflection as its refractive index lies between ALON and air. The high strength and extended service life of PMMA protect the critical components of electrochromic windows from corrosion. Fig. 8(a) shows the schematic of the electrochromic window with four bias voltages (EW-4) deposited on a SiO_2 substrate and protected by a PMMA coating. The d_{PMMA} , d_{Subs} , d_{DAST} , and d_{ALON} of PMMA, SiO_2 substrate, DAST, and ALON are set to 50 nm, 5 mm, 100 nm, and 20 nm, respectively. Fig. 8(b) displays the relationship between T_{vis} , T_{IR} , and CRI and the four bias voltages. The T_{vis} and T_{IR} adjustable ranges for the EW-4 are 72.5% – 92.3% and 46.1% – 95.2%, respectively. In Fig. 8(b), without bias voltage, point P_0 (88.7%, 81.7%, 99) shows good performance of the electrochromic window. Remembering that the three numbers in parentheses represent the point's T_{vis} , T_{IR} , and CRI, and similar expressions can be found in the following. Point P_A (77.2%, 94.7%, 90) corresponds to mode - I with lower T_{vis} and higher T_{IR} . Mode - II, represented by point P_B (83.6%, 94.5%, 94), allows for maximum visible and IR light transmission. Point P_C (80.2%, 46.1%, 95) shows mode - IV, which has high T_{vis} but low T_{IR} to minimize temperature rises while maintaining visible light in the summer. The electrochromic glass has its lowest transmission values at point P_D (75.6%, 46.1%, 95). However, P_D does not meet mode - III requirements. Nevertheless, EW-4 has significant practical value for independently modulating visible and IR transmission.

The CRI is calculated by comparing the color rendering of the test source to that of a perfect source, a black body radiator for sources with correlated color temperatures under 5000 K. An ideal CRI value is 100, indicating that the smart window's transmission light can accurately reveal the colors of various objects compared to the perfect source [37]. A CRI value of not less than 90 is regarded as excellent, whereas a value of less than 80 is generally considered poor [38]. The proposed smart window must have a CRI value of more than 90 in practical applications. Consider the EW-4 configuration shown in Fig. 8(a), which depicts 4651 states in Fig. 8(b). The T_{vis} and T_{IR} values of P_E and P_F are nearly comparable in the partially enlarged view of Fig. 8(c). Since the bias voltages of P_E (82.3%, 93.4%, 89) and P_F (82.3%, 93.4%, 96) are different, they have different CRI (89 and 96, respectively). When T_{vis} and T_{IR} have been determined, if the CRI value is low, one can choose the higher value of CRI from Fig. 8(c). However, as depicted in Fig. 8(d), the CRI in the region near the P_G (74.7%, 90.4%, 82) is poor, which requires sacrificing either T_{vis} or T_{IR} values to ensure that the CRI is not below a certain

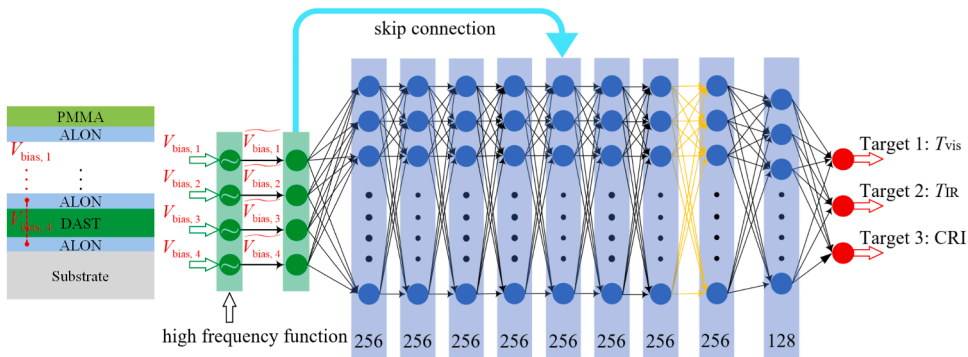


Fig. 6. The fully-connected network architecture, with input vectors in green, intermediate hidden layers in blue, and output vectors in red. The number inside each block represents the vector dimension. Black arrows indicate layers with rectified linear unit (ReLU) activations, while orange arrows indicate those without ReLU activations. The cyan arrow shows the skip connection. (For interpretation of the references to color in this figure legend, the reader is referred to the web version of this article.)

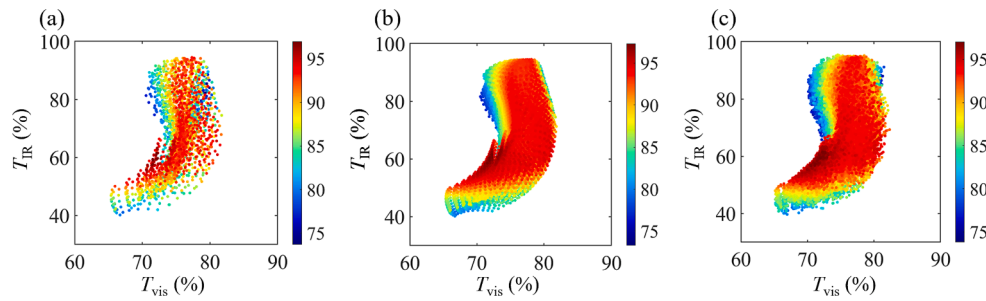


Fig. 7. The T_{vis} , T_{IR} , and CRI for 4651 (a) and 61,051 (b) states calculated by TMM. (c) The network model predicted the T_{vis} , T_{IR} , and CRI for 61,051 states.

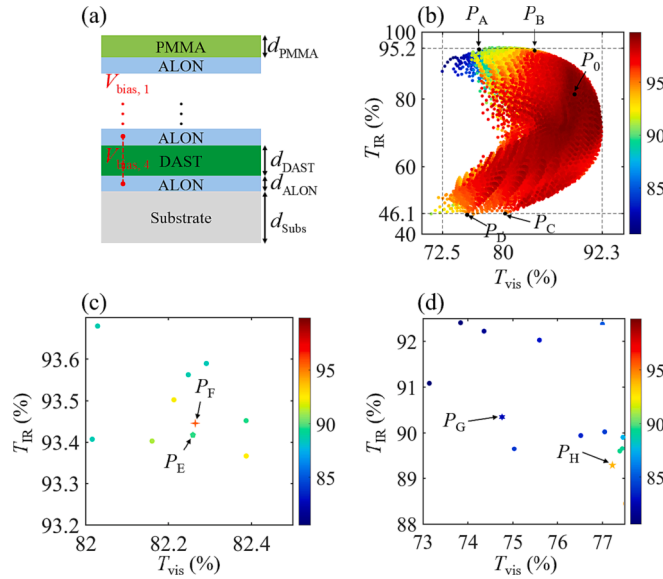


Fig. 8. (a) The schematic diagram of the multilayer structure of an electrochromic window with four bias voltages. (b) The T_{vis} , T_{IR} , and CRI versus each bias voltage. (c) and (d) offer enlarged views of (b).

threshold. Therefore, individuals can substitute the P_G with the P_H (77.2%, 89.3%, 94). For convenience, the states with high CRI are displayed first in this work's T_{vis} - T_{IR} figure, whereas Figure S2 (Supporting Information) illustrates the states with low CRI shown first in the T_{vis} - T_{IR} figure.

5.2. Comparison with recent work

Fig. 9 compares this work with newly published theoretical simulation electrochromic windows [16–19] and a classical passive window [39]. It is worth noting that because CRI is not mentioned in these papers, the CRI of these smart windows is not provided in Fig. 9. The performance of these electrochromic windows has been reported. Still,

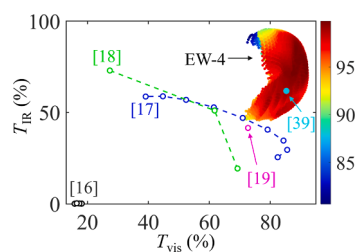


Fig. 9. (a) Comparison of the EW-4 structure with recently reported theoretical simulation electrochromic windows [16–19] and a classic passive window [39]. The area with display CRI is the EW-4 structure's regulation range.

their regulation of T_{vis} and T_{IR} is not independent, and few meet practical demands. In this work, the EW-4 achieves independent regulation of T_{vis} and T_{IR} , with a large regulation range (T_{vis} ranging from 65.9% to 87.6% and T_{IR} ranging from 41.1% to 93.9%), which is superior to recently reported works. The structure's modulation range is notably more extensive and exhibits exceptional visible and IR light modulation.

5.3. Synthetic discussion

Through the above discussion, the proposed electrochromic window with multiple bias voltages can regulate T_{vis} and T_{IR} independently. The range of regulation gradually increases with the increase of the number of bias voltages. However, the present structure is composed of lossless material, leading to the smart window not performing well in mode - III. As the number of calculations increases, the fully-connected network based on position coding can significantly reduce simulation time while maintaining prediction accuracy. If the CRI is below a particular value, an increase in CRI can be achieved by changing the bias voltages without changing the values of T_{vis} and T_{IR} as shown in Fig. 8(c). When the above method fails, the CRI can only be ensured to be greater than a particular value by sacrificing the value of T_{vis} and T_{IR} as shown in Fig. 8(d). Compared to previously reported work, the present EW-4 has a wider regulation range of visible and IR light. Moreover, the structure is independent of polarization and easy to fabricate, which offers significant promise for future smart window applications.

6. Conclusion

In summary, we propose a DAST-based multilayer film structure for energy-saving windows that can effectively and independently regulate T_{vis} and T_{IR} . When applying different bias voltages, the refractive index and impedance of the multilayer DAST films change accordingly, allowing independent control of the visible and IR light range. The electrochromic windows with four bias voltages can exhibit an excellent regulation range (T_{vis} ranging from 72.5 to 92.3%, and T_{IR} ranging from 46.1 to 95.2%), outperforming recently reported works. A position coding-based fully-connected network is proposed, which accelerates the simulation through truth prediction data. This loss-free multilayer film construction for smart windows is independent of polarization, easy to fabricate, and holds significant promise for future energy-saving window applications.

CRedit authorship contribution statement

Xueyu Wang: Writing – review & editing, Validation, Supervision, Project administration. **Shuo Chen:** Writing – review & editing. **Yumin Liu:** Writing – review & editing, Validation, Supervision, Project administration, Funding acquisition. **Tiesheng Wu:** Writing – review & editing, Validation, Supervision, Project administration, Funding acquisition. **Jing Li:** Writing – review & editing, Supervision. **Danfeng Zhu:** Writing – review & editing, Supervision. **Yuhang Sun:** Writing – review & editing, Supervision. **Hongjie Fan:** Writing – review & editing,

Supervision.

Declaration of Competing Interest

The authors declare that they have no known competing financial interests or personal relationships that could have appeared to influence the work reported in this paper.

Data availability

Data will be made available on request.

Acknowledgments

This research was funded by the National Natural Science Foundation of China (NSFC) (61875021); Natural Science Foundation of Beijing (2192036); The Fundamental Research Funds for the Central Universities; Guangxi Key Laboratory of Wireless Wideband Communication and Signal Processing; BUPT Action Plan Project (ZDYY202102-1).

Appendix A. Supplementary data

Supplementary data to this article can be found online at <https://doi.org/10.1016/j.optlastec.2023.109774>.

Reference

- [1] Total Energy Annual Data - U.S. Energy Information Administration (EIA), (n.d.). <https://www.eia.gov/totalenergy/data/annual/> (accessed February 6, 2023).
- [2] Y. Ke, J. Chen, G. Lin, S. Wang, Y. Zhou, J. Yin, P.S. Lee, Y. Long, Smart windows: Electro-, thermo-, mechano-, photochromics, and beyond, *Adv. Energy Mater.* 9 (2019) 1902066, <https://doi.org/10.1002/aenm.201902066>.
- [3] A. Khatibi, M. Hossein Jahangir, F. Razi Astaraei, Energy and comfort evaluation of a novel hybrid control algorithm for smart electrochromic windows: A simulation study, *Sol. Energy* 241 (2022) 671–685, <https://doi.org/10.1016/j.solener.2022.06.045>.
- [4] K. Tang, K. Dong, J. Li, M.P. Gordon, F.G. Reichertz, H. Kim, Y. Rho, Q. Wang, C.-Y. Lin, C.P. Grigoropoulos, A. Javey, J.J. Urban, J. Yao, R. Levinson, J. Wu, Temperature-adaptive radiative coating for all-season household thermal regulation, *Science* 374 (2021) 1504–1509, <https://doi.org/10.1126/science.abf7136>.
- [5] Y. Du, S. Liu, Z. Zhou, H.H. Lee, T.C. Ho, S.-P. Feng, C.Y. Tso, Study on the halide effect of MA4PbX₆-2H₂O hybrid perovskites – From thermochromic properties to practical deployment for smart windows, *Mater. Today Phys.* 23 (2022), 100624, <https://doi.org/10.1016/j.mtphys.2022.100624>.
- [6] L. Wang, Y. Liu, X. Zhan, D. Luo, X. Sun, Photochromic transparent wood for photo-switchable smart window applications, *J. Mater. Chem. C* 7 (2019) 8649–8654, <https://doi.org/10.1039/C9TC02076D>.
- [7] S.-Y. Chun, S. Park, S.I. Lee, H.D. Nguyen, K.-K. Lee, S. Hong, C.-H. Han, M. Cho, H.-K. Choi, K. Kwak, Operando Raman and UV-Vis spectroscopic investigation of the coloring and bleaching mechanism of self-powered photochromic devices for smart windows, *Nano Energy* 82 (2021), 105721, <https://doi.org/10.1016/j.nanoen.2020.105721>.
- [8] S. Zhang, S. Cao, T. Zhang, J.Y. Lee, Plasmonic oxygen-deficient TiO₂-x nanocrystals for dual-band electrochromic smart windows with efficient energy recycling, *Adv. Mater.* 32 (2020) 2004686, <https://doi.org/10.1002/adma.202004686>.
- [9] A. Cots, S. Dicorato, L. Giovannini, F. Favoino, M. Manca, Energy efficient smart plasmochromic windows: properties, manufacturing and integration in insulating glazing, *Nano Energy* 84 (2021), 105894, <https://doi.org/10.1016/j.nanoen.2021.105894>.
- [10] X. Wang, M. Li, D. Wang, H. Zhang, R. Duan, D. Zhang, B. Song, B. Dong, Low-cost, robust pressure-responsive smart windows with dynamic switchable transmittance, *ACS Appl. Mater. Interfaces* 12 (2020) 15695–15702, <https://doi.org/10.1021/acsami.0c00300>.
- [11] J. Wang, C. Meng, C.-T. Wang, C.-H. Liu, Y.-H. Chang, C.-C. Li, H.-Y. Tseng, H.-S. Kwok, Y. Zi, A fully self-powered, ultra-stable cholesteric smart window triggered by instantaneous mechanical stimuli, *Nano Energy* 85 (2021), 105976, <https://doi.org/10.1016/j.nanoen.2021.105976>.
- [12] J. Hoon Lee, J. Jeong, Y. Tae Chae, Optimal control parameter for electrochromic glazing operation in commercial buildings under different climatic conditions, *Appl. Energy* 260 (2020), 114338, <https://doi.org/10.1016/j.apenergy.2019.114338>.
- [13] D.-K. Bui, T.N. Nguyen, A. Ghazlan, T.D. Ngo, Biomimetic adaptive electrochromic windows for enhancing building energy efficiency, *Appl. Energy* 300 (2021), 117341, <https://doi.org/10.1016/j.apenergy.2021.117341>.
- [14] A. Georg, A. Georg, Electrochromic device with a redox electrolyte, *Sol. Energy Mater. Sol. Cells* 93 (2009) 1329–1337, <https://doi.org/10.1016/j.solmat.2009.02.009>.
- [15] A.M. Österholm, L. Nhon, D.E. Shen, A.M. Dejneka, A.L. Tomlinson, J.R. Reynolds, Conquering residual light absorption in the transmissive states of organic electrochromic materials, *Mater. Horiz.* 9 (2022) 252–260, <https://doi.org/10.1039/D1MH01136G>.
- [16] M. Aalizadeh, A.E. Serebryannikov, A. Khavasi, G.A.E. Vandenbosch, E. Ozbay, Toward electrically tunable, lithography-free, ultra-thin color filters covering the whole visible spectrum, *Sci. Rep.* 8 (2018) 11316, <https://doi.org/10.1038/s41598-018-29544-x>.
- [17] A.K. Chowdhary, D. Sikdar, Design of electrotunable all-weather smart windows, *Sol. Energy Mater. Sol. Cells* 222 (2021), 110921, <https://doi.org/10.1016/j.solmat.2020.110921>.
- [18] A.K. Chowdhary, D. Sikdar, Multilayer thin-film based nanophotonic windows: static versus electrotunable design, *J. Opt.* 24 (2022), 024002, <https://doi.org/10.1088/2040-8986/ac3eb0>.
- [19] A.K. Chowdhary, T. Bhowmik, J. Gupta, D. Sikdar, Energy-saving all-weather window based on selective filtering of solar spectral radiation, *Appl. Opt.* 60 (2021) 1315, <https://doi.org/10.1364/AO.412932>.
- [20] A. Forouzmmand, H. Mosallaei, Electro-optical amplitude and phase modulators based on tunable guided-mode resonance effect, *ACS Photonics* 6 (2019) 2860–2869, <https://doi.org/10.1021/acsphotonics.9b00950>.
- [21] S. Park, H.S. Park, T.T. Dao, S.H. Song, S.I. Lee, H.V. Tran, A. Ullah, C.-H. Han, S. Hong, Solvothermal synthesis of oxygen deficient tungsten oxide nano-particle for dual band electrochromic devices, *Sol. Energy Mater. Sol. Cells* 242 (2022), 111759, <https://doi.org/10.1016/j.solmat.2022.111759>.
- [22] D. Ma, A. Lee-Sie Eh, S. Cao, P.S. Lee, J. Wang, Wide-spectrum modulated electrochromic smart windows based on MnO₂/PB films, *ACS Appl. Mater. Interfaces* 14 (2022) 1443–1451, <https://doi.org/10.1021/acsami.1c20011>.
- [23] Reference Air Mass 1.5 Spectra | Grid Modernization | NREL, (n.d.). <https://www.nrel.gov/grid/solar-resource/spectra-am1.5.html> (accessed February 6, 2023).
- [24] C.C. Katsidis, D.I. Siapkas, General transfer-matrix method for optical multilayer systems with coherent, partially coherent, and incoherent interference, *Appl. Opt.* 41 (2002) 3978–3987, <https://doi.org/10.1364/AO.41.003978>.
- [25] H.A.M.A. Macleod, *Thin-film optical filters, Fourth Edition*, Taylor and Francis; CRC Press, 2010.
- [26] E.-T. Hu, X.-X. Liu, Y. Yao, K.-Y. Zang, Z.-J. Tu, A.-Q. Jiang, K.-H. Yu, J.-J. Zheng, W. Wei, Y.-X. Zheng, R.-J. Zhang, S.-Y. Wang, H.-B. Zhao, O. Yoshie, Y.-P. Lee, C.-Z. Wang, D.W. Lynch, J.-P. Guo, L.-Y. Chen, Multilayered metal-dielectric film structure for highly efficient solar selective absorption, *Mater. Res. Express* 5 (2018), 066428, <https://doi.org/10.1088/2053-1591/aacdb3>.
- [27] A.K. Chowdhary, D. Sikdar, Low-power design of electrotunable color filters and optical switches, *J. Opt. Soc. Am. B* 37 (2020) 3865, <https://doi.org/10.1364/JOSAB.408502>.
- [28] W. Geis, R. Sinta, W. Mowers, S.J. Deneault, M.F. Marchant, K.E. Krohn, S. J. Spector, D.R. Calawa, T.M. Lyszczarz, Fabrication of crystalline organic waveguides with an exceptionally large electro-optic coefficient, *Appl. Phys. Lett.* 84 (2004) 3729–3731, <https://doi.org/10.1063/1.1723697>.
- [29] M. Ramisetty, S. Sastri, U. Kashalikar, L.M. Goldman, N. Nag, Transparent polycrystalline cubic spinels protect and defend, *American Ceramics Society, Bulletin* 92 (2013) 20–25.
- [30] T.M. Hartnett, S.D. Bernstein, E.A. Maguire, R.W. Tustison, Optical properties of ALON (aluminum oxynitride), *Infrared Phys. Technol.* 39 (1998) 203–211, [https://doi.org/10.1016/S1350-4495\(98\)00007-3](https://doi.org/10.1016/S1350-4495(98)00007-3).
- [31] X. Zhang, J. Qiu, X. Li, J. Zhao, L. Liu, Complex refractive indices measurements of polymers in visible and near-infrared bands, *Appl. Opt.* 59 (2020) 2337–2344, <https://doi.org/10.1364/AO.383831>.
- [32] E. Hecht, *Optics 4th Edition*, Optics. (1998).
- [33] D.M. Pozar, *Microwave engineering*, John Wiley & sons, 2011.
- [34] S. Mao, J. Liu, Y. Pan, J. Lee, Z. Yao, P. Pandey, S. Kunwar, Z. Zhu, W. Shen, L. A. Belfiore, J. Tang, Morphological and optical evolution of metallic oxide/Au nanoparticle hybrid thin film: High absorption and reflectance by plasmonic enhancement, *Appl. Surf. Sci.* 495 (2019), 143575, <https://doi.org/10.1016/j.apsusc.2019.143575>.
- [35] S. So, Y. Yang, T. Lee, J. Rho, On-demand design of spectrally sensitive multiband absorbers using an artificial neural network, *Photon. Res.* 9 (2021) B153, <https://doi.org/10.1364/PRJ.415789>.
- [36] B. Mildenhall, P.P. Srinivasan, M. Tancik, J.T. Barron, R. Ramamoorthi, R. Ng, NeRF: representing scenes as neural radiance fields for view synthesis, *Commun. ACM* 65 (2022) 99–106, <https://doi.org/10.1145/3503250>.
- [37] Color rendering index, Wikipedia. (2022). https://en.wikipedia.org/wiki/Color_rendering_index (accessed March 5, 2023).
- [38] What is CRI? The ultimate guide to the Color Rendering Index | Waveform Lighting, (n.d.). <https://www.waveformlighting.com/tech/what-is-cri-color-rendering-index> (accessed February 16, 2023).
- [39] L.V. Besteiro, X.-T. Kong, Z. Wang, F. Rosei, A.O. Govorov, Plasmonic glasses and films based on alternative inexpensive materials for blocking infrared radiation, *Nano Lett.* 18 (2018) 3147–3156, <https://doi.org/10.1021/acs.nanolett.8b00764>.